

An experimentally realizable single-atom chaotic driven top in silicon

Vincent Mourik,^{1,*} Serwan Asaad,^{1,*} Hannes Fircgau,¹ Jarryd J. Pla,² Catherine Holmes,³ Gerard J. Milburn,⁴ Jeffrey C. Mccallum,⁵ and Andrea Morello¹

¹*Centre for Quantum Computation and Communication Technologies,
School of Electrical Engineering and Telecommunications,
UNSW Sydney, Sydney, New South Wales 2052, Australia*

²*School of Electrical Engineering and Telecommunications,
UNSW Sydney, Sydney, New South Wales 2052, Australia*

³*School of Mathematics and Physics, The University of Queensland, St Lucia, Brisbane 4072, Australia*

⁴*ARC Centre of Excellence for Engineered Quantum Systems, School of Mathematics and Physics,
The University of Queensland, St Lucia, Brisbane 4072, Australia*

⁵*Centre for Quantum Computation and Communication Technology,
School of Physics, University of Melbourne, Melbourne VIC 3010, Australia*

(Dated: March 16, 2017)

Among the many controversial aspects of the quantum / classical boundary, the emergence of chaos remains amongst the least experimentally verified. In particular, the time-resolved observation of quantum chaotic dynamics, and its interplay with quantum measurement, is largely unexplored outside experiments in atomic ensembles. We present here a realistic proposal to construct a chaotic driven top from the nuclear spin of a single donor atom in silicon, in the presence of nuclear quadrupole interaction. This system is exquisitely measurable and controllable, and possesses extremely long intrinsic quantum coherence times, allowing for the observation of subtle dynamical behavior over extended periods. We show that signatures of chaos are expected to arise for experimentally realizable parameters of the system, allowing the study of the relation between quantum decoherence and classical chaos, and the observation of dynamical tunneling.

I. INTRODUCTION

The correspondence principle, as formulated by the Copenhagen school of quantum mechanics, states that the dynamics of quantum systems should converge towards classical dynamics, in the limit where the system becomes large. Appealing (and, for simple cases, often correct) as it may sound, this point of view is afflicted by a plethora of complications and controversies around the precise nature of the quantum / classical transition,¹ such as decoherence² and the quantum measurement problem.³ Another key aspect of the quantum / classical transition concerns the question of reconciling the chaotic dynamics of certain classical systems with the unitary evolution of their quantum-mechanical counterparts. On the one hand, the classical Liouville equation has the property of conserving phase space volume, which can be seen as the equivalent of the quantum unitary dynamics arising from the Schrödinger equation. On the other hand, the discrete spectrum of quantum systems prevents ‘true’ chaos from occurring,⁴ since quantum systems exhibit quasiperiodicity, and the uncertainty principle smooths out the fine structure in the classical phase space⁵ that would result in the exponential sensitivity of chaotic systems to the initial conditions. Therefore, it is often stated that ‘quantum chaos’ constitutes a new and unique type of dynamics.⁶

The issue of how to observe and interpret signatures of chaos in quantum mechanics has profound repercussions on many important topics in physics. For example, classical chaos underpins the ergodic hypothesis in statistical mechanics, and it is expected that its quantum equivalent plays a fundamental role in the thermalization of isolated

quantum systems.^{7–9} Chaos is also thought to be related to the issue of decoherence,¹⁰ which is crucial in the modern topic of quantum information science. There, one must answer the delicate question of whether an onset of chaos may harm the operation of a large-scale quantum computer.^{11–13}

Despite its broad and deep importance, experimental progress in ‘quantum chaos’ is rare. Early work focused on the study of static and statistical properties of chaotic systems, such as the energy spectra of chaotic billiards implemented in semiconductor quantum dots.^{14,15} Even more rare is the ability to experimentally observe *dynamical* chaos, i.e. signatures of chaos in the time evolution of quantum systems. Crudely speaking, this is because most quantum systems decohere and randomize for trivial reasons (noise, uncontrolled environments, etc.) over time scales that are too short for signatures of chaotic behavior to reveal themselves. The experimental state of the art is found in ensembles of cold gases,^{16–18} whereas only very recently an experiment on three superconducting qubits has revealed the link between chaos and thermalization in a small-scale quantum system.¹⁹ What is still missing is an experimental study of the quantum signatures of chaos in an *individual* quantum system. Ensemble experiments provide approximations of the Hamiltonian of quantum chaotic systems, but their validity sometimes relies upon neglecting interactions within the ensemble. More importantly, a single quantum object is best suited to study the interplay between the emergence of chaos and the measurements performed on the system.^{20,21}

Here we present a detailed and quantitative proposal to experimentally realize a single-atom version of one of the

best studied quantum chaotic systems, the ‘kicked top’.²² For experimental convenience, we will focus on the case where the top is periodically driven, instead of kicked with δ -functions. This system becomes chaotic in the presence of a term in the Hamiltonian that is quadratic in the angular momentum. The obvious quantum equivalent of a classical spinning top is a spin. The challenge here is to find a spin system whose Hamiltonian maps onto that of the chaotic driven top (in particular, it must have a quadratic term in the spin operators), while retaining intrinsic quantum coherence for very long times.

Our proposed system is the nuclear spin of a heavy group-V substitutional donor in isotopically enriched ²⁸Si.²³ The lightest group-V donor in silicon, ³¹P, has been extensively studied in the context of quantum information processing,²⁴ since it naturally contains two quantum bits, the electron (with spin $S = 1/2$) and the ³¹P nucleus (with spin $I = 1/2$). High-fidelity single-shot readout,^{25,26} coherent operation,^{26,27} mutual entanglement²⁸ and variable-strength measurements²⁹ have been experimentally demonstrated. When implanted³⁰ in isotopically enriched ²⁸Si, these single-atom spins exhibit outstanding coherence times³¹ (up to 35 seconds for the nuclear spin) and control fidelities.^{32,33} This suggests that donor spin systems would be ideal platforms to study the subtle effects of dynamical chaos and its interplay with quantum measurement, if it were possible to engineer a suitable spin Hamiltonian. This is not the case with ³¹P, since its spin value of $1/2$ forbids the presence of quadratic terms in the Hamiltonian. Heavier donors, such as ⁷⁵As, ¹²¹Sb, ¹²³Sb and ²⁰⁹Bi, all have nuclear spin $I > 1/2$, which allows the presence of a nuclear quadrupole interaction. Below we show that, under realistic conditions of quadrupole coupling and period drive, a heavy group-V donor can become a single-atom solid-state implementation of a chaotic driven top.

The paper is organized as follows: in Section II we review the chaotic dynamics of a classical driven top; Section III describes in detail the requirements to realize the quantum version of a chaotic top; Section IV shows how to implement it in the nuclear spin of a group-V donor in silicon; Section V provides a quantitative analysis of the Hamiltonian parameters available with different donor choices; Section VI compares the classical and the quantum dynamics of the top and the spin; Section VII gives conclusions and outlook. Details on the classical equations of motion, Floquet formalism, useful properties of spins $I > 1/2$, classical vs. quantum Hamiltonian parameters, nuclear quadrupole interaction, NMR spectroscopy, state preparation and readout, and numerical methods are given in appendices.

II. CLASSICAL DYNAMICS OF THE DRIVEN TOP

The periodically driven top is a rigid body having finite angular momentum about its center of mass, $\mathbf{L} =$

$(L_x \ L_y \ L_z)^T$, $|\mathbf{L}| = \text{constant}$, subject to a harmonic drive. It constitutes a modified version of the kicked top, which is one of the best studied examples of classically chaotic dynamical systems. In order to display chaos, the minimal Hamiltonian \mathcal{H} of the driven top takes the form:

$$\mathcal{H}_{\text{classical}} = \alpha L_z + \beta L_x^2 + \gamma L_y \cos(2\pi f t), \quad (1)$$

with α , β , and γ proportionality constants, and f the frequency of the drive. The term βL_x^2 provides an energy contribution that is nonlinear in the angular momentum, and is key to the emergence of dynamical chaos. The classical equations of motion of this system are derived in App. A.

Chaos is revealed by drawing a stroboscopic Poincaré map, i.e. the locus of $\mathbf{L}(nT)$ on the sphere of radius L , with $T = 1/f$, $n = 0, 1, \dots, N$ and N the total number of periods of the applied drive. Repeating the analysis for a large number of initial conditions reveals a partition of the sphere in regular regions where the points $\{\mathbf{L}(nT)\}$ accumulate along periodic orbits, and chaotic regions where $\{\mathbf{L}(nT)\}$ disperse across wide regions with no periodicity, and an exponential sensitivity of the trajectory to the precise initial condition (Fig. 1a).

Around the x -axis, the quadratic term in Eq. 1 dominates the dynamics, giving rise to two closed regions of regular motion in the southern hemisphere near $+\hat{x}$ and $-\hat{x}$ (no trajectories shown). Similarly, the linear term produces a regular region of precession around $+\hat{z}$ (blue trajectory). Inside these regions, the periodic drive does not significantly affect the axis of precession. Outside the regular regions, the periodic drive in combination with the quadratic term cause a ‘twist’ of the trajectories, resulting in chaotic trajectories (red dots), highly sensitive to perturbations.

The size and shape of the regular and chaotic regions is determined by the Hamiltonian parameters α , β , γ , and f (Fig. 1). Since the dynamics depend on the relative parameter strengths, α is used as a fixed scale for the other parameters. Decreasing β makes the quadratic stable regions shrink and veer towards $-\hat{z}$, whereas increasing β expands these regions towards $+\hat{x}$ and $-\hat{x}$ (Fig. 1b, c). The chaotic fraction is largest when $\beta \approx \alpha$. Increasing (decreasing) the periodic drive strength γ results in an enlargement (reduction) of the chaotic region (Fig. 1d, e). The size of the chaotic region further depends on the drive frequency f , and is largest when f is chosen near the precession frequency of trajectories at the boundaries of regular regions ($f \approx 1.4\alpha$ when $\alpha \approx \beta$) (Fig. 1f, g). A detailed study of the chaotic fraction of phase space as a function of the different parameters confirms these trends (Fig. 1h, i).

In summary, a sizable region of chaos is found with linear and quadratic interactions of similar strength ($\beta \approx \alpha$), a sufficiently strong periodic drive strength ($\gamma \gtrsim 0.02\alpha$), and a drive frequency near resonance ($f \approx 1.4\alpha$). These are the conditions we seek to reproduce in the quantum driven top.

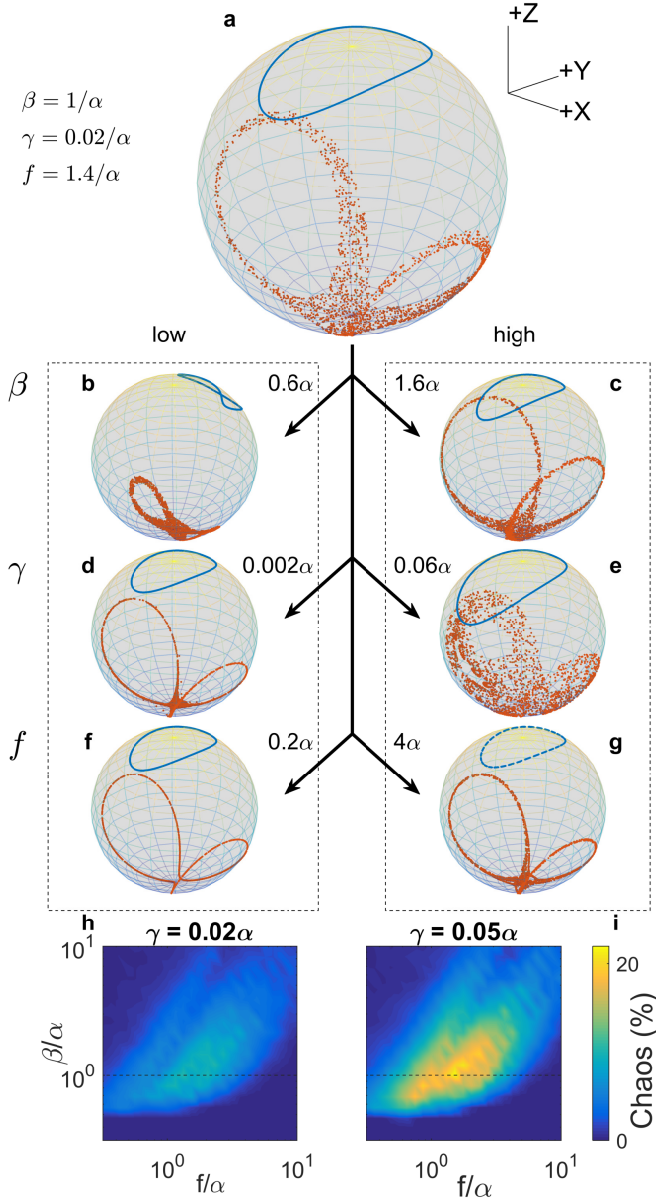


Figure 1. Dynamics of the classical driven top (Eq. 1). (a) Stroboscopic map of two trajectories of \mathbf{L} corresponding to initial conditions in a regular (blue) and chaotic (red) region, with parameters shown to the left. (b-g) Same as (a), but where a single parameter is varied. (b,c) Modifying the quadratic interaction strength β shrinks the chaotic region and displaces the enclosed regular regions. (d,e) Increasing (decreasing) the periodic drive strength γ leads to an enlarged (reduced) chaotic region. (f,g) Shifting the drive frequency f away from precession frequencies at the boundaries of regular regions results in a reduced chaotic region. (h,i) Chaotic percentage of total phase space as a function of quadratic interaction strength and periodic drive frequency for weak [(h), $\gamma = 0.02\alpha$] and strong [(i), $\gamma = 0.05\alpha$] periodic drive strength (App. H). Dashed horizontal lines indicate $\beta = \alpha$.

III. REQUIREMENTS FOR A QUANTUM DRIVEN TOP

We present a strategy to obtain an experimentally realizable quantum-mechanical equivalent of the driven top described by Eq. (1). For this purpose, the classical angular momentum \mathbf{L} is replaced by a spin with spin quantum number I , and magnetic quantum number $m \in [-I, -I + 1, \dots, I - 1, I]$ and corresponding spin operators $\mathbf{I} = (I_x \ I_y \ I_z)^T$.

A useful correspondence with the classical Hamiltonian imposes several conditions.

(i) *Large spin number, $I > 1/2$.* Although one can in principle write the pure state of a spin with arbitrary precision, the Heisenberg uncertainty principle prevents such a state from being reliably distinguishable from another state, unless they are orthogonal. Therefore, one cannot imagine the state of a quantum spin as a point on a sphere, but must blur the point with an area of uncertainty of at least order \hbar . This is visually depicted using, for example, the Husimi Q representation (App. C 2). Since \hbar is constant and the surface of the sphere of constant angular momentum increases quadratically with I , the *relative* uncertainty in localizing the direction of the spin vector decreases by increasing I . For $I = 1/2$, \hbar covers a whole hemisphere, rendering any concept of trajectory largely meaningless. The minimum uncertainty states are known as spin coherent states, where the condition $|\mathbf{I}| = \sqrt{\langle I_x \rangle^2 + \langle I_y \rangle^2 + \langle I_z \rangle^2} \leq I$ becomes an equality (App. C 1). They can be thought of as the equivalent of minimum-uncertainty Gaussian wave packets for the description of a particle in position and momentum space. Here, the spin coherent states represent the closest quantum-mechanical approximation of a classical angular momentum state.

(ii) *A spin Hamiltonian of the same form as that of a classically chaotic driven top*, thus including a linear term (for example a Zeeman energy for a spin in a magnetic field), a periodic drive, and a quadratic term in the spin operators. In addition, we seek quantum systems where the Hamiltonian can be tuned (preferably *in situ*) to attain the combination of parameters that map the classical chaotic driven top, with relative strengths appropriate for the emergence of chaos.

(iii) *Access to high-fidelity single-shot state readout, and/or variable-strength weak measurements.* The ability to perform single-shot readout or stroboscopically probe the state of a driven spin opens the possibility of studying details of the interplay between chaos and quantum measurement. This is a crucial and largely unexplored aspect of quantum chaos, which has been largely inaccessible to experiments due to the ensemble nature of most experiments to date.

(iv) *Long intrinsic quantum coherence time.* We seek to unravel subtle features in the time evolution of a quantum system that maps on the classically chaotic driven top. It is of paramount importance that the system does not

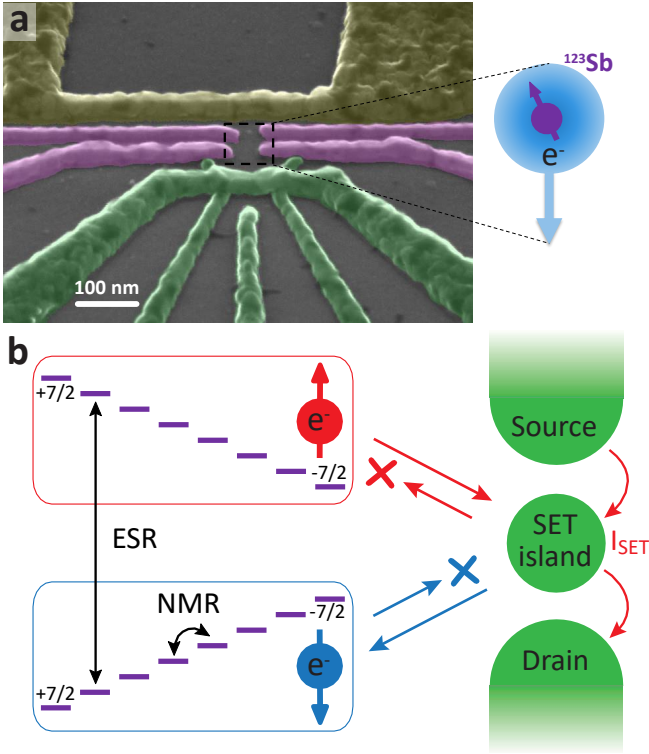


Figure 2. Experimental implementation of the quantum driven top. (a) Scanning electron microscope image of a typical device. ^{123}Sb donors can be implanted in the ^{28}Si epilayer in the indicated position. Their electrochemical potential is controlled by electrostatic gates (false colored in pink), and a single-electron transistor (green) is fabricated in the vicinity of the donor implant area, to provide time-resolved electron spin readout via spin-dependent tunneling. A broadband microwave antenna (yellow) provides oscillating magnetic fields to excite the electron (ESR) and nuclear (NMR) resonances, and to periodically drive the nuclear spin. (b) The 16 energy levels of the ^{123}Sb donor (spacings not to scale), separated into the electron spin-down (blue) and spin-up (red) manifold. For electron spin readout, the donor electrochemical potential is tuned such that only the $|\uparrow\rangle$ state can tunnel out of the donor, while only the $|\downarrow\rangle$ can tunnel back on it. The SET is tuned such that the current is nonzero when the donor is ionized.

lose coherence for trivial reasons, unrelated to chaos, on time scales short compared to the chaotic dynamics.

IV. A SINGLE NUCLEAR SPIN IN SILICON AS A QUANTUM DRIVEN TOP

The quantum equivalent of a periodically driven top, satisfying all the conditions listed in the previous section, can be built using the nuclear spin of a single group-V donor in silicon with $I > 1/2$, i.e. all group-V elements except phosphorus.

At low temperatures, group-V donors in silicon bind an extra electron, whose spin $S = 1/2$ is described by the

vector of operators $\mathbf{S} = (S_x \ S_y \ S_z)^T$, while the nuclear spin is described by $\mathbf{I} = (I_x \ I_y \ I_z)^T$.

Neglecting the nuclear quadrupole interaction (discussed later), the spin Hamiltonian of the electron-nuclear system in the presence of a static magnetic field B_0 in the z -direction and an oscillating magnetic field B_1 at frequency f in the y -direction reads:

$$\mathcal{H} = (\gamma_e S_z - \gamma_n I_z) B_0 + A \mathbf{S} \cdot \mathbf{I} + \dots \quad (2)$$

$$\dots + (\gamma_e S_y - \gamma_n I_y) B_1 \cos(2\pi f t),$$

where γ_e and γ_n are the electron and nuclear gyromagnetic ratios (their magnetic moments have opposite sign), and A is the hyperfine interaction between electron and nuclear spin, assumed to be isotropic. The oscillating B_1 field allows for coherent control of the spins through electron spin resonance (ESR) and nuclear magnetic resonance (NMR), as well as the application of numerous techniques for tomography and characterization of the spin system.³⁴

In the limit where the electron Zeeman term is much larger than the hyperfine interaction ($\gamma_e B_0 \gg A$), the hyperfine interaction is well approximated by $A S_z I_z$, and it is possible to write an effective nuclear spin Hamiltonian as

$$\mathcal{H} = (-\gamma_n B_0 \pm \frac{1}{2} A) I_z - \gamma_n I_y B_1 \cos(2\pi f t). \quad (3)$$

The state of the electron spin only determines the sign of the $\pm \frac{1}{2} A$ term, which acts effectively as a classical magnetic field, dependent on the electron state. The donor can also be operated in the ionized state, in which case the hyperfine contribution $\pm \frac{1}{2} A I_z$ vanishes from Eq. 3.

This electron-nuclear spin system is operated and read out using a nanoelectronic device (Fig. 2) which can be fabricated on an isotopically enriched ^{28}Si epilayer in order to minimize the decoherence arising from the ^{29}Si nuclear spin bath.^{31,35} Donors with $I > 1/2$ will be shallowly implanted in a small ($\leq 100 \text{ nm} \times 100 \text{ nm}$) lithographically-defined window, in close proximity to local electrostatic gates that define a single-electron transistor (SET). The electrochemical potential of the donor-bound electron is controlled by additional electrostatic gates (App. G).

State preparation and measurement rely on spin-dependent tunneling of the electron to and from the SET island.²⁵ This method requires the electron Zeeman splitting $\gamma_e B_0$ to be large compared to the thermal broadening of the SET island's Fermi distribution (of order $5k_B T$, where k_B is the Boltzmann's constant and T is the temperature). For electron temperatures $T \approx 100 \text{ mK}$, as routinely obtainable in dilution refrigerators, the lowest admissible field for reliable initialization and readout is of order 0.5 T . This will become important when discussing the parameter range where chaotic behavior can be observed.

The hyperfine interaction A couples the electron and the nuclear spins, introducing a dependence of the ESR frequency on the state of the nucleus. This, in turn, allows the measurement (and consequent initialization by measurement) of the nuclear spin state by observing at

what frequency the electron spin responds to a resonant microwave excitation.²⁶ A broadband on-chip antenna supplies the required oscillating magnetic field B_1 , in the GHz (ESR) and MHz (NMR) frequency ranges.³⁶ These features enable the full initialization, control, and readout of both electron and nuclear spin (App. G).

When applied to the nuclear spin of the ^{31}P donor, this setup has delivered state preparation and readout with better than 99.9% fidelity. The use of isotopically purified ^{28}Si and the operation of the nuclear spin in the ionized state results in exceptionally long dephasing times ($T_{2n0}^* = 0.6\text{ s}$) and even longer coherence times in the presence of dynamical decoupling ($T_{2n0}^{\text{CPMG}} = 35.6\text{ s}$).³¹ These performance benchmarks make nuclear spins in ^{28}Si excellent systems to observe subtle dynamical phenomena over long time scales, as desirable for the study of chaotic dynamics. To do so, however, we need to include in the spin Hamiltonian an additional term, quadratic in the spin operators. Such a term arises naturally by using nuclei with $I > 1/2$, which possess nonzero quadrupole moment.

The nuclear quadrupole moment is caused by the non-spherical charge distribution of the nucleus. This quadrupole interacts with electric field gradients to introduce a new term in the spin Hamiltonian.³⁷ In general, the tensor describing the electric field gradient can be diagonalized to $\text{diag}(V_{x'x'}, V_{y'y'}, V_{z'z'})$ by an appropriate choice of coordinate frame (x', y', z') , where $V_{ij} = \frac{\partial^2 V}{\partial i \partial j}$, ($i, j \in x', y', z'$) are the partial second derivatives of the electrostatic potential V , and $|V_{x'x'}| \leq |V_{y'y'}| \leq |V_{z'z'}|$. The expression for the nuclear quadrupole interaction is then simplified to³⁸

$$\mathcal{H}_Q = Q \left(I_{z'}^2 - \frac{I^2}{3} + \frac{\eta}{3} (I_{x'}^2 - I_{y'}^2) \right), \quad (4)$$

where Q is the effective quadrupole interaction strength, which scales linearly with both $V_{z'z'}$ and the nuclear quadrupole moment Q_n (App. E), and the asymmetry parameter $\eta = \frac{V_{x'x'} - V_{y'y'}}{V_{z'z'}}$ quantifies the deviation from axial symmetry of the electric field gradient ($0 \leq \eta \leq 1$, $\eta = 0$ corresponds to axial symmetry).

The important features of the quadrupole interaction are that it is quadratic in the spin operators and has a preferred quantization axis. Assuming that the static magnetic field B_0 can be oriented in an arbitrary direction (for example using a 3-axis vector magnet) and that the electric field gradient has axial symmetry ($\eta = 0$), the linear and quadratic terms in the spin Hamiltonian can be made orthogonal. Ignoring the static energy offset $QI^2/3$, and assuming for simplicity that the symmetry axis of the electric field gradient is orthogonal to the periodic driving field B_1 , the Hamiltonian of a donor with nuclear spin $I > 1/2$ takes the form:

$$\mathcal{H}_{\text{quantum}} = (\gamma_n B_0 \pm \frac{1}{2}A) I_z + QI_x^2 + \gamma_n B_0 \cos(2\pi ft) I_y. \quad (5)$$

Therefore, $\mathcal{H}_{\text{quantum}}$ represents the quantum equivalent

Table I. Parameters of group-V donors in silicon. 1s binding energies taken from Ref. 39. Hyperfine interaction A taken from Ref. 40. Nuclear gyromagnetic ratio $\gamma_n = \mu\mu_n/I$ is calculated from the nuclear magnetic moment μ given in units of nuclear magneton $\mu_n = 7.62\text{ MHz/T}$ in Ref. 41. Minimum and maximum values of nuclear quadrupole moment Q_n are given, based on the range of values reported in Ref. 41.

donor	I	1s binding energy (meV)	A (MHz)	γ_n (MHz/T)	Q_n (10^{-28} m^2)
^{31}P	1/2	45.59	117.53	17.26	-
^{75}As	3/2	53.76	198.35	7.31	0.314
^{121}Sb	5/2	42.74	186.80	10.26	[-0.36, -0.54]
^{123}Sb	7/2	42.74	101.52	5.55	[-0.49, -0.69]
^{209}Bi	9/2	70.98	1475.4	6.96	[-0.37, -0.77]

of the Hamiltonian of a classical periodically-driven top (Eq. 1).

V. SUITABLE DONORS AND PREFERRED OPERATION REGIMES

We now analyze in detail how to estimate quantitatively the parameters of the spin Hamiltonian of the quantum driven top, in order to compare them to the parameters that are known to lead to chaotic dynamics in the equivalent classical case.

The key parameter values of the group-V donors with $I > 1/2$ are summarized in Table I. The value of I increases with atomic mass, while the hyperfine interaction A has a non-monotonic behavior, with a significant jump for the heavy ^{209}Bi donor. Large I values are desirable to reduce the quantum uncertainty on the spin state, whereas from the analysis of the classical driven top we know that interesting chaotic dynamics arises when linear and quadratic terms in the spin Hamiltonian are of comparable strength.

For operation in the neutral charge state, the linear term has strength $\gamma_n B_0 \pm A/2$, which becomes very large in the case of ^{209}Bi where $A = 1475.4\text{ MHz}$. The $\pm A/2$ contribution can be removed by operating in the ionized state. The nuclear Zeeman term is minimized by operating at low B_0 , with the caveat that reducing B_0 affects the electron readout and initialization fidelity. Using $B_0 = 0.5\text{ T}$ and ionized donors, the linear term in the spin Hamiltonian thus takes values of order 3 MHz.

Next, we wish to obtain a comparable value for the quadratic term, which is achieved by maximizing the strength of the quadrupole interaction, and hence the electric field gradient (Eq. 4). In bulk silicon, the nuclear quadrupole interaction vanishes due to the cubic symmetry of the crystal lattice. However, the implanted donor is not in bulk silicon, but close to a Si/SiO₂ interface and underneath a stack of Al electrodes for control and readout. Crucially, aluminum has a significantly larger thermal expansion coefficient than silicon. Upon cooling the device from ambient to sub-Kelvin temperatures, this

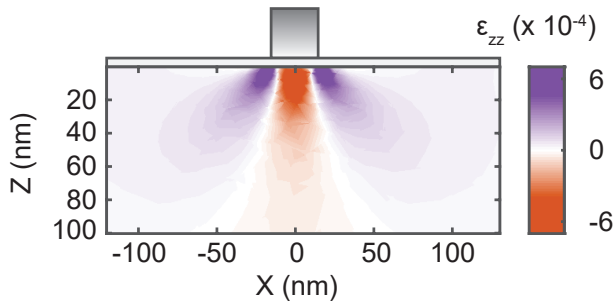


Figure 3. Finite-elements model of the strain induced in silicon at low temperatures by a $30 \times 30 \text{ nm}^2$ aluminum gate, placed on top of a 5 nm thick SiO_2 dielectric. The maximum strain approaches 0.1%.

causes a significant strain of the underlying silicon lattice.^{42,43} Finite-elements models of the strain caused by Al gates on top of a Si/ SiO_2 stack indicate that strain values approaching 0.1% can be expected (Fig. V). The disruption of the cubic lattice symmetry under the metal results in an electric field gradient at the donor site. This electric field gradient is further enhanced at the nucleus due to rearrangement of the closed electronic shells of the donor (Sternheimer anti-shielding effect^{37,44}). These effects are present in both the neutral and the ionized charge state, albeit with different strengths.

Measurements of the quadrupole interaction strength of group-V donors in strained silicon, especially near a nano-structure interface, have only been conducted very recently. In the case of ionized donors near the Si/ SiO_2 /Al interface, the available data in Refs. 43, 45–47 only allows an order of magnitude estimate of $Q \sim 300 \text{ kHz}$ for ionized ^{209}Bi (App. E). Note that when comparing the classical and quantum systems, both \mathbf{L} and quantum operators \mathbf{I} need to be normalized, and therefore the coefficient β in the classical Hamiltonian must be compared to QI in the quantum case (App. D). This makes the value $Q \sim 300 \text{ kHz}$ rather promising, since the corresponding $QI \sim 1 \text{ MHz}$ is within an order of magnitude of the linear interaction strength ($\gamma_n B_0 \sim 3 \text{ MHz}$). If this proves to be insufficient, strain engineering⁴⁸ could be deployed to further increase the electric field gradient to reach the target value of $QI \sim 3 \text{ MHz}$. For the purpose of studying the chaotic dynamics of a nuclear spin as a function of its Hamiltonian parameters, an appealing approach is the introduction of piezoelectric elements on the silicon chip. Notably, strain causes both an increased quadrupole interaction and a decreased hyperfine coupling,⁴⁹ thus affecting directly the ratio between linear and quadratic Hamiltonian terms.

The broadband antenna near the donor can be used to apply a radio-frequency periodic drive. Previous work has been conducted with drive strengths up to $B_1 \sim 2 \text{ mT}$,²⁶ which correspond to radiofrequency powers of order 0.5 mW (at the chip). Those values were sufficient

to achieve high-fidelity coherent control of the ^{31}P nuclear spin qubit. Here, we wish to compare $\gamma_n B_1$ to the classical parameter γ . Chaos arises when $\gamma \approx 0.02\alpha$ in the classical model. For $B_0 \sim 0.5 \text{ T}$ and thus $\alpha \sim 3 \text{ MHz}$, this requires $B_1 \sim 10 \text{ mT}$. Assuming the same setup and antenna as Ref.,²⁶ this value would require $\sim 10 \text{ mW}$ radiofrequency power at the chip. This is a very high value for operation at millikelvin temperatures, but we note that the broadband microwave antenna is terminated by a short circuit, constituting (ideally) a fully reflective load. Therefore, only a small fraction of the incident power is actually dissipated on the chip, while the rest is reflected and dissipated upstream. Alternatively, high B_1 values with low incident power could be obtained by using LC resonators, at the expense of broad frequency tunability.

In summary, these estimates suggest that the ^{123}Sb and ^{209}Bi donors in silicon are suitable candidates to implement the quantum driven top, due to their high spin quantum number ($I = 7/2$ and $I = 9/2$, respectively), low nuclear gyromagnetic ratio ($\gamma_n = 5.55 \text{ MHz T}^{-1}$ and $\gamma_n = 6.96 \text{ MHz T}^{-1}$) and, in the case of ^{123}Sb , low hyperfine coupling strength ($A = 101.52 \text{ MHz}$). ^{123}Sb has the additional advantage that its suitability for ion implantation is well documented:⁵⁰ after low-energy implantation and high-temperature rapid thermal anneal, the Sb atoms are fully activated, and the implantation damage to the silicon lattice is thoroughly repaired. Recent work⁵¹ suggests that the implantation damage can be efficiently repaired also in the case of ^{209}Bi , although the electrical activation yield remains lower than that of Sb. The attainable quadrupole interaction is not well known, but recent work^{43,45,46} indicates that it can plausibly reach a comparable value to the nuclear Zeeman term in low ($B_0 \sim 0.5 \text{ T}$) static magnetic field. When combined with a strong oscillating magnetic field ($B_1 \sim 10 \text{ mT}$), we conclude that the parameter range where the equivalent classical driven top behaves chaotic throughout sizable areas of its phase space is within reach. In what follows, we will concentrate our discussion on the use of ^{123}Sb as the model system to study quantum chaos in a single spin.

VI. QUANTUM VERSUS CLASSICAL DYNAMICS: A COMPARISON

To illustrate the applicability of the ^{123}Sb system to the study of quantum chaos, we propose two types of experiments: one aimed at finding a correspondence between the classically chaotic driven top and its quantum counterpart, the other at demonstrating a violation of classical dynamics, exposing the true quantum nature of the system.

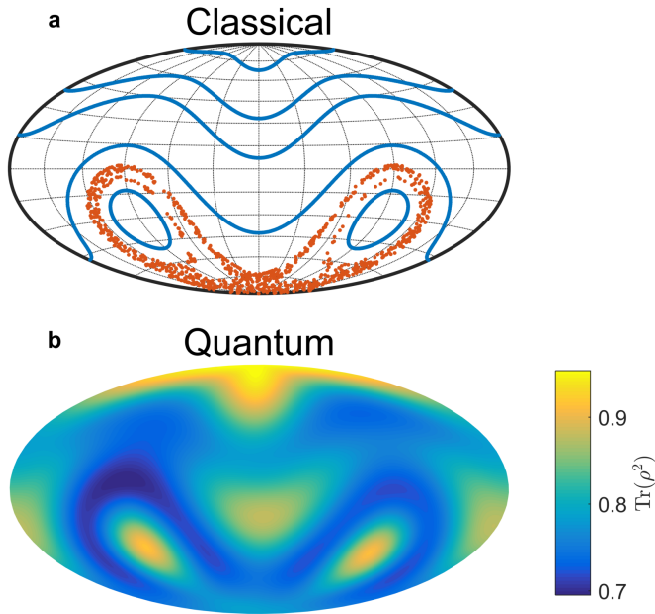


Figure 4. Comparison between classical Poincaré map and quantum state purity of a periodically driven top. The spherical surfaces of constant angular momentum are visualized by Hammer projections. (a) Classical: stroboscopic map of one chaotic trajectory (red) and six regular trajectories (blue) for $N = 1000$ sampling periods, with the same simulation parameters as Fig. 1a, i.e. $\beta = 1/\alpha$, $\gamma = 0.02/\alpha$, $f = 1.4/\alpha$. The chaotic region divides the three regular regions and contains regular trajectories within their respective regions. (b) Quantum: Purity of spin coherent states $|\theta, \phi\rangle$ of an ionized ^{123}Sb atom with $I = 7/2$, $\gamma_n = 5.55 \text{ MHz T}^{-1}$, $B_0 = 0.5 \text{ T}$, $Q = 800(2) \text{ kHz}$, $B_1 = 10 \text{ mT}$, $f = 3.5 \text{ MHz}$. The state purity is extracted from the density matrix ρ , which is obtained by evolving each spin coherent state for $N = 1000$ drive periods while randomly perturbing Q once per drive period, and averaging over 200 such evolutions (App. H). The maps show a correspondence between the purity of spin coherent quantum states and regular / chaotic structure of the classical phase space.

A. Decoherence as a precursor of chaos

Classical chaos is characterized by an extreme sensitivity to perturbations, and as a consequence, neighboring trajectories with slightly different initial coordinates rapidly diverge (Sec. II). This is in stark contrast with quantum dynamics, where the discrete nature of the energy spectrum results in quasi-periodic behavior, leading to partial revivals of the initial quantum state instead (App. B). However, quantum states evolving under slightly perturbed Hamiltonians do experience divergence. Since a quantum system is never truly isolated, interactions with its environment lead to unknown perturbations of the Hamiltonian, effectively entangling the system with its environment. The unknown nature of this process translates to the quantum state losing its purity, thus decohering into a mixed state.

Crucial to the quantum driven top, certain initial quan-

tum states are more prone to decoherence, while others remain relatively unperturbed. This behavior appears related to the high sensitivity of certain classical states to perturbations, but is caused here by a varying sensitivity of the time-evolution operator's eigenstates to perturbations (App. B). States containing more of these high-sensitivity eigenstates are therefore more susceptible to phase errors. In line with this picture, Zurek and co-workers¹⁰ predict that the rate at which different initial quantum states decohere provides a mapping to the (non-)chaotic nature of the corresponding classical system, with chaotic classical regions corresponding to more rapidly decohering initial quantum states.

The driven-top system can be used to verify this prediction, both through simulations and experiments. By evolving an initial state for a certain duration using the driven-top Hamiltonian (Eq. 5), the resulting density matrix ρ provides information about the degree of decoherence through its purity $\text{Tr}(\rho^2)$. Decoherence is simulated by randomly varying a Hamiltonian parameter during the state's evolution, and calculating the state purity from the ensemble average of many final states, each obtained with a different randomized evolution (App. H). By sampling over all spin coherent states, a 'purity map' of the quantum driven top is obtained, which we compare to its classical counterpart (Fig. 4). The simulations highlight a correspondence between the classically-chaotic regions and quantum regions of strong decoherence, and between classically-regular regions and quantum regions of weak decoherence. To experimentally verify these predictions, we aim to prepare spin coherent states (App. G), evolve the system under the driven-top Hamiltonian, and finally reconstruct ρ_{final} using quantum state tomography. Repeating this for different initial spin coherent states allows for experimental reconstruction of the 'purity map', which can then be compared to the corresponding classical phase space.

B. Dynamical tunneling

In the absence of a periodic drive, trajectories of the classical top are closed orbits confined to distinct regions in a two-dimensional phase space (the surface of a sphere due to $|\mathbf{L}|$ being a constant of motion). Upon addition of a periodic drive, this behavior is largely kept intact, except near boundaries between the regular regions, where a chaotic behavior appears. The classically-separated regions of regular motion have an analogue in the corresponding quantum system, where they can be identified as region of weak decoherence (Fig. 4). However, there is a fundamental difference between the quantum and the classical case. In the classical system, the Kolmogorov, Arnol'd and Moser (KAM) theorem ensures that a system initially prepared within one of the regular regions will remain on a period orbit within such region. The quantum system, however, cannot be precisely localized within a certain region, due to the uncertainty principle. The 'leak-

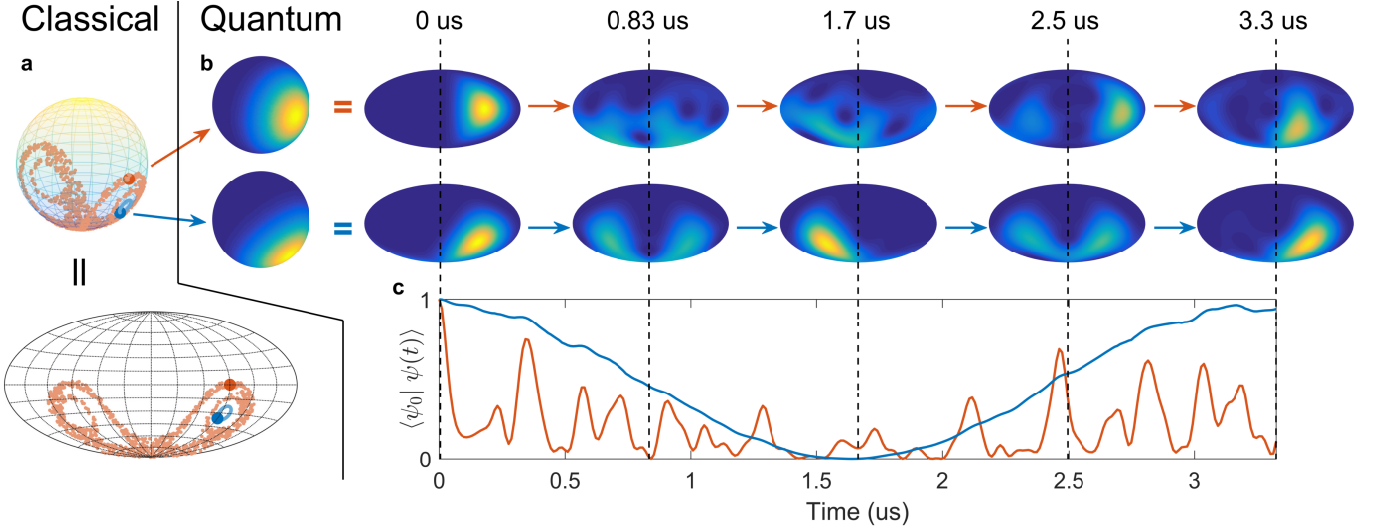


Figure 5. Time evolution of the quantum driven top. Two different initial spin coherent states are chosen in the directions of a classically chaotic region (red) and a classically regular region (blue). Implementation in a $I = 7/2$ nuclear spin of an ionized ^{123}Sb donor in silicon with $\gamma_n = 5.55 \text{ MHz T}^{-1}$, $B_0 = 0.5 \text{ T}$, $Q = 0.8 \text{ MHz}$, $B_1 = 10 \text{ mT}$, $f = 5 \text{ MHz}$. (a) Classical angular-momentum trajectories with initial states corresponding to orientations of spin coherent states and parameters matching the quantum simulations (Table II). Trajectories are visualized by both a three-dimensional spherical plot (top) and Hammer projection (bottom), with enlarged dots representing the two initial angular-momentum coordinates. (b) Husimi Q representation (App. C 2) of the two spin coherent states at different moments in their evolutions (see App. H for simulation details). Top (bottom) row corresponds to spin coherent state oriented in the direction of the classically chaotic (regular) region in phase space, specified by orange (blue). In both rows, the first colormap is a three-dimensional view of the initial spin coherent state, equal to the first Hammer projection. The subsequent Hammer projections show the evolution of the quantum state at later times. The spin coherent state prepared in the classically chaotic region (top) displays a rapid dispersion over the phase space, while the classically regular spin coherent state (bottom) transfers back and forth between two classically regular regions. This property is known as dynamical tunneling, and is in stark contrast with classical dynamics, where trajectories cannot cross closed regions. (c) Overlap of the time-evolved state $|\psi(t)\rangle$ with its initial state $|\psi(0)\rangle$ for spin coherent states in classically chaotic (orange) and regular (blue) regions. Dynamical tunneling (blue) is revealed by a near-sinusoidal evolution of the overlap, returning to near unity. This is in contrast to the evolution of the classically-chaotic spin coherent state, where the overlap quickly decreases and does not display a revival.

age' of the quantum wavefunction into a different regular region results in the phenomenon of dynamical tunneling, i.e. the tunneling of the quantum state between separate regular regions, in violation of the KAM theorem.

Dynamical tunneling manifests itself in the quantum driven top as a periodic oscillation of a spin coherent state between the two classically-regular regions associated with the quadratic interaction (Fig. 5a). In contrast, a spin coherent state prepared within a classically chaotic region rapidly loses purity and shows no apparent revival to a spin coherent state (Fig. 5b, c).

Numerical simulations, conducted using Hamiltonian parameters appropriate for ^{123}Sb , clearly show the appearance of dynamical tunneling for spin coherent states prepared initially within the regions of classically regular periodic orbits (Fig. 5b, c). The predicted period of dynamical tunneling is $\sim 3 \mu\text{s}$. This is a crucial result, since this period is orders of magnitude shorter than the dephasing time of a nuclear spin in ^{28}Si ,³¹ ensuring that the coherent dynamical tunneling oscillations can be observed in an experiment over unprecedented time scales.

VII. CONCLUSION AND OUTLOOK

We have shown how the high-spin nucleus of a single donor in silicon is an experimentally realizable platform to study the transition from quantum to classical dynamics, and in particular the emergence of chaos and its interplay with decoherence. The system and its operation build upon many years of scientific and technological development in silicon single-atom devices for quantum information processing, and adds new functionalities for the study of fundamental problems in physics.

We have focused here on the single-atom nature of the system, which makes it unique as a platform for the study of dynamical quantum chaos. We note, however, that all the efforts directed towards building a large-scale quantum processor based on ^{31}P can be applied to building an equivalent system in ^{123}Sb . New methods for electrical control, electric dipole and microwave cavity coupling of donor electron-nuclear spin states⁵² could be extended to the ^{123}Sb system in the chaotic regime, providing insight into the interplay between chaos and multi-qubit operations, as well as allowing continuous and

variable-strength dispersive readout. This, in turn, could open up the prospect of applying the toolbox of quantum trajectories⁵³ to chaotic systems in the solid state.

ACKNOWLEDGMENTS

We thank A. Laucht, F.A. Mohiyaddin, V. Schmitt and G. Tosi for suggestions and comments. This work was funded by an Australian Research Council Discovery Project (DP150101863). VM acknowledges support from a Niels Stensen Fellowship.

Appendix A: Derivation of classical equations of motion

The general expressions for the equations of motion of the driven top are given here. Starting point is Hamilton's equation of motion in Poisson bracket formulation:

$$\frac{d\mathbf{L}}{dt} = \{\mathbf{L}, \mathcal{H}\} + \frac{\partial \mathbf{L}}{\partial t} \quad (\text{A1})$$

with $\mathbf{L} = (L_x \ L_y \ L_z)^T$ the angular momentum vector, \mathcal{H} the Hamiltonian, and $\{\mathbf{L}, \mathcal{H}\}$ the Poisson bracket relation between \mathbf{L} and \mathcal{H} . Angular momentum conservation implies $\partial \mathbf{L} / \partial t = 0$. Introducing $\dot{L}_i \equiv dL_i / dt$, the equations of motion are:

$$\begin{aligned} \dot{L}_x &= \{L_x, \mathcal{H}\} \\ \dot{L}_y &= \{L_y, \mathcal{H}\} \\ \dot{L}_z &= \{L_z, \mathcal{H}\} \end{aligned} \quad (\text{A2})$$

1. Equations of motion for the classical driven top

The equations of motion given above can be applied to the classical driven top (Eq. 1). As an example, we derive an expression for \dot{L}_y

$$\begin{aligned} \dot{L}_y &= \{L_y, \alpha L_z + \beta L_x^2 + \gamma L_y \cos(2\pi ft)\} \\ &= \alpha \underbrace{\{L_y, L_z\}}_{=L_x} + \beta \{L_y, L_x^2\} + \gamma \cos(2\pi ft) \underbrace{\{L_y, L_y\}}_{=0} \\ &= \alpha L_x - \beta \underbrace{\{L_x, L_y\} L_x}_{=L_z} - \beta L_x \underbrace{\{L_x, L_y\}}_{=L_z} \\ &= \alpha L_x - 2\beta L_x L_z \end{aligned} \quad (\text{A3})$$

where the product rule for Poisson brackets is used in the third line and whenever Poisson brackets are computed, the relation $\{L_i, L_j\} = \epsilon_{ijk} L_k$, with ϵ_{ijk} the Levi-Cevita symbol, is used. Similarly, equations for L_x and L_z can be derived, resulting in the system of equations

$$\begin{aligned} \dot{L}_x &= -\alpha L_y + \gamma L_z \cos(2\pi ft) \\ \dot{L}_y &= \alpha L_x - 2\beta L_x L_z \\ \dot{L}_z &= -2\beta L_x L_y - \gamma L_x \cos(2\pi ft). \end{aligned} \quad (\text{A4})$$

Appendix B: Quantum dynamics and Floquet formalism

The evolution of time-dependent periodic Hamiltonians, such as the quantum driven top (Eq. 5), can be transformed to time-independent evolutions using the Floquet formalism. The Floquet operator F is equal to the time evolution operator \mathcal{U} over one full period τ

$$F \equiv \mathcal{U}(\tau, 0) = \int_0^\tau e^{-it\mathcal{H}(t)/\hbar} dt, \quad (\text{B1})$$

As a result, the Floquet operator F has the property $|\psi(\tau)\rangle = F |\psi(0)\rangle$, irrespective of the state $|\psi\rangle$. A consequence is that $|\psi(N\tau)\rangle = F^N |\psi(0)\rangle$, and so once F is known, any state can be straightforwardly evolved over a discrete number of periods by repeated application of F .

The Floquet operator can be decomposed into eigenstates $|\Phi_i\rangle$ and corresponding eigenvalues λ_i , which all satisfy $|\lambda_i| = 1$ (F is unitary). All eigenvalues are therefore of the form $\lambda_i = \exp(-i\epsilon_i\tau/\hbar)$, where the angular frequency ϵ_i is known as the quasienergy of the corresponding eigenstate. This enables decomposition of any initial state $|\psi(0)\rangle$ into the Floquet eigenstates, and straightforward calculation of its state after evolution of N periods

$$\begin{aligned} |\psi(N\tau)\rangle &= F^N |\psi(0)\rangle \\ &= \sum_i \langle \Phi_i | \psi(0) \rangle F^N |\Phi_i\rangle \\ &= \sum_i \langle \Phi_i | \psi(0) \rangle \exp(-i\epsilon_i N\tau/\hbar) |\Phi_i\rangle \end{aligned} \quad (\text{B2})$$

Each Floquet eigenstate accumulates a phase determined by its respective quasienergy, and so superpositions of eigenstates will lead to interference effects. This offers an explanation for the evolution of spin coherent states (Fig. 5), where the spin coherent state with many Floquet components (orange) has many interfering frequencies, while the state that exhibits dynamical tunneling (blue) primarily consists of two Floquet components, and consequently two main interfering frequencies. The Floquet formalism also connects to the varying dephasing rates for different initial states (Fig. 4), as the individual Floquet quasienergies have a different degree of sensitivity to perturbations. More generally, the Floquet formalism clearly emphasizes the discrete nature of quantum mechanics, leading to quasi-periodicity that causes partial revivals of initially localized states, as opposed to the exponential divergence of trajectories in the case of classical chaos.

Appendix C: Spin $I > 1/2$: some properties and definitions

1. Spin coherent states

Spin coherent states, also known as Bloch states, form a subset of the possible states of a spin- I system. The for-

mulation and some relevant properties of the spin coherent states are reviewed here.

For a spin with spin quantum numbers I and magnetic quantum number $m \in [-I, -I+1, \dots, I-1, I]$, states can be described by the basis states $|I, m\rangle$, which are eigenstates of the I_z spin operator with corresponding eigenvalue m .

We introduce spherical angles ϕ (azimuthal) and θ (polar), and an operator $R_{\theta, \phi}$ corresponding to a rotation over an angle θ about an axis $(\sin \phi, -\cos \phi, 0)$, given by:

$$R_{\theta, \phi} = e^{-i\theta(I_x \sin \phi - I_y \cos \phi)} \quad (C1)$$

The spin coherent states $|\theta, \phi\rangle$ are now defined as the state $|I, I\rangle$ rotated by $R_{\theta, \phi}$:⁵⁴

$$\begin{aligned} |\theta, \phi\rangle &= R_{\theta, \phi} |I, I\rangle \\ &= \sum_{m=-I}^I \binom{2I}{I+m}^{1/2} e^{i\phi(I-m)} \times \dots \\ &\dots \times (\cos \tfrac{1}{2}\theta)^{I+m} (\sin \tfrac{1}{2}\theta)^{I-m} |I, m\rangle \end{aligned} \quad (C2)$$

All spin coherent states share the property

$$|\mathbf{I}| = \sqrt{\langle I_x \rangle^2 + \langle I_y \rangle^2 + \langle I_z \rangle^2} = I \quad (C3)$$

Furthermore, the spin coherent states form an overcomplete normalized basis, having non-zero overlap with each other. Only opposite spin coherent states with a π difference in polar angle θ are orthogonal and have zero overlap, analogous to the orthogonality of $|I, -I\rangle$ and $|I, I\rangle$.

Rotated spin operators can be obtained by applying $R_{\theta, \phi}$ to the original spin operators

$$\begin{aligned} I_{x'} &= R_{\theta, \phi} I_x R_{\theta, \phi}^{-1}, \\ I_{y'} &= R_{\theta, \phi} I_y R_{\theta, \phi}^{-1}, \\ I_{z'} &= R_{\theta, \phi} I_z R_{\theta, \phi}^{-1}, \end{aligned} \quad (C4)$$

in which case the spin coherent state is an eigenstate of $I_{z'}$ with eigenvalue I . Spin coherent states are the only states for which the uncertainty relation $(\sigma_{I_{x'}}^2, \sigma_{I_{y'}}^2 \geq \frac{\hbar}{4} \langle I_{z'} \rangle^2)$ becomes an equality, and are therefore also known as minimum-uncertainty states.

The concept of spin coherent states is not necessary in the case $I = 1/2$, since all pure states are spin coherent states. However, for $I > 1/2$ the spin coherent states are the subset of states for which the spin is maximally aligned in a certain direction (θ, ϕ) , and has a minimum-uncertainty spread around it. As such, these states are the closest analogue to a classical angular momentum, and are therefore used in the quantum driven top experiments as corresponding initial quantum states.

2. Husimi Q distribution

The Husimi Q distribution is a quasiprobability distribution that is used to represent quantum states. It

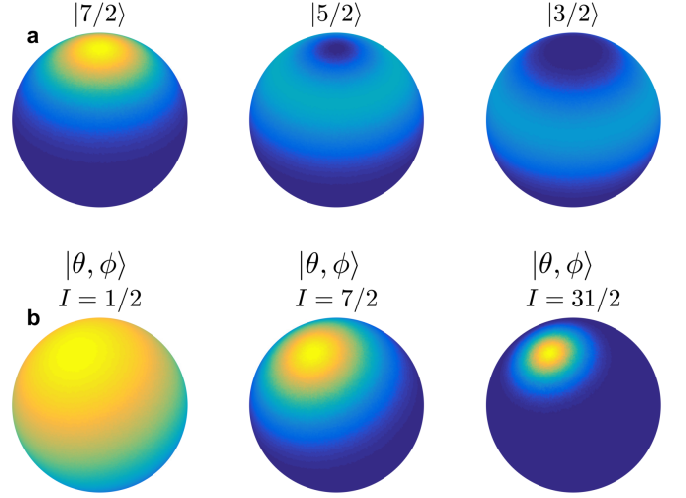


Figure 6. Husimi representation of quantum states. Each point on the sphere surface corresponds to the Husimi Q function (Eq. C5) evaluated at those spherical coordinates. Color-scale limits are constant over all panels. (a) Visualization of three eigenstates of I_z for $I = 7/2$. Whereas the state $|7/2\rangle$ is a spin coherent state oriented along $+z$ with minimum uncertainty, as can be seen by its small spread over the spherical surface, the other two eigenstates are uniform bands with a larger spread since these are not minimum-uncertainty states. (b) Visualization of a spin coherent state for increasing I . In the limiting case $I = 1/2$, the uncertainty spread nearly covers the entire sphere. As I is increased, the relative uncertainty of the coherent state decreases, resulting in the state being more localized.

is particularly useful here to provide a visualization of high-dimensional quantum states (Fig. 6). For a given density matrix ρ , the Husimi Q function is defined as

$$Q(\theta, \phi) = \frac{1}{\pi} \langle \theta, \phi | \rho | \theta, \phi \rangle, \quad (C5)$$

where $|\theta, \phi\rangle$ is a spin coherent state. In the case of a pure state ($\rho = |\psi\rangle \langle \psi|$), the Husimi Q distribution simplifies to $Q(\theta, \phi) = \frac{1}{\pi} |\langle \psi | \theta, \phi \rangle|^2$, the overlap-squared between $|\psi\rangle$ and $|\theta, \phi\rangle$.

The Husimi Q distribution satisfies certain properties required for a joint probability distribution, because the distribution is normalized and non-negative with values ranging between $0 \leq Q(\theta, \phi) \leq 1/\pi$. However, since different spin coherent states are nonorthogonal, different coordinates (θ, ϕ) do not represent distinct physical contingencies, and different values of Q are not the probability of mutually exclusive states, a requirement for a joint probability distribution. This reflects the fact that quantum mechanics lacks a clear phase-space description, as opposed to classical mechanics. However, quasiprobability distributions such as the Husimi Q distribution are a complete representation of a quantum state, and are invertible to the original density matrix representation.

The Husimi Q distribution is preferred here over the Wigner distribution as the phase space representation of

quantum states because classical effects are emphasized. For instance, application of the Husimi Q function to a spin coherent state closely matches a classical point in phase space with the addition of an uncertainty spread (Fig. 6b). A downside is that typical quantum phenomena such as interference are not clearly visible. To study these effects, other distributions such as the Wigner distribution are more attractive candidates.

3. Uncertainty and size of I

Spin coherent states are the set of minimum uncertainty states ($\sigma_{I_x}^2, \sigma_{I_y}^2 = \frac{\hbar}{4} \langle I_z \rangle^2 = \frac{\hbar}{4} I^2$). Its uncertainty defines a typical area over which a coherent state spreads in phase space, and should be compared to the total surface of the phase space ($4\pi I^2$). This leads to a concept of relative uncertainty $\sigma_{I_x} \sigma_{I_y} / 4\pi I^2 \propto 1/I$, which is a measure of how well a quantum state is localized in phase space. This underlines the importance of having large enough I , as illustrated by comparing the Husimi Q function of spin coherent states for different I (Fig. 6b). Having $I = 7/2$ or larger is necessary to effectively localize a quantum state in a corresponding classical region, and observe phenomena such as dynamical tunneling.

Appendix D: Classical and quantum Hamiltonian parameters

The classical simulation results shown in Fig. 1 use dimensionless parameters which eases a direct comparison to corresponding dimensionless parameters in the quantum case. Here, their relation to the parameters in the original Hamiltonian (Eq. (1)) and to the corresponding quantum parameters is given.

1. Rescaling of classical Hamiltonian parameters

Both the variables (\mathbf{L}, t) and the parameters $(\alpha, \beta, \gamma, f)$ need a dimensionless equivalent. Dividing the classical Hamiltonian \mathcal{H}_c by $|\mathbf{L}|$ (including a factor 2π to convert from rad s^{-1} to Hz) we obtain

$$\begin{aligned} \frac{\mathcal{H}_c}{2\pi|\mathbf{L}|} &= \frac{\alpha}{2\pi} \frac{L_z}{|\mathbf{L}|} + \frac{\beta}{2\pi} \frac{L_x^2}{|\mathbf{L}|} + \frac{\gamma}{2\pi} \cos(2\pi f t) \frac{L_y}{|\mathbf{L}|} \\ &= \frac{\alpha}{2\pi} L'_z + \frac{\beta}{2\pi} |\mathbf{L}| L'^2_x + \frac{\gamma}{2\pi} \cos(2\pi f t) L'_y, \end{aligned} \quad (\text{D1})$$

where the normalized angular momentum variable $\mathbf{L}' = \mathbf{L}/|\mathbf{L}|$ is introduced. Next we divide by $\alpha/2\pi$ and time $t' = (\alpha/2\pi)t$ is introduced:

$$\begin{aligned} \mathcal{H}'_c &= \frac{\mathcal{H}_c}{\alpha|\mathbf{L}|} = L'_z + \frac{\beta|\mathbf{L}|}{\alpha} L'^2_x + \frac{\gamma}{\alpha} \cos\left(2\pi \frac{2\pi f}{\alpha} t'\right) L'_y \\ &= L'_z + \beta' L'^2_x + \gamma' \cos(2\pi f' t') L'_y \end{aligned} \quad (\text{D2})$$

Table II. Comparison of equivalent classical and quantum Hamiltonian parameters.

classical		quantum	
original	dimensionless	original	dimensionless
\mathbf{L}	$\mathbf{L}' = \frac{\mathbf{L}}{ \mathbf{L} }$	\mathbf{I}	$\mathbf{I}' = \frac{\mathbf{I}}{I}$
$\frac{\alpha}{2\pi}$	1	$\gamma_n B_0$	1
$\frac{\beta}{2\pi}$	$\beta' = \frac{\beta \mathbf{L} }{\alpha}$	Q	$Q' = \frac{QI}{\gamma_n B_0}$
$\frac{\gamma}{2\pi}$	$\gamma' = \frac{\gamma}{\alpha}$	$\gamma_n B_1$	$B'_1 = \frac{B_1}{B_0}$
f	$f' = \frac{2\pi f}{\alpha}$	f	$f' = \frac{f}{\gamma_n B_0}$
t	$t' = \frac{\alpha}{2\pi} t$	t	$t' = \gamma_n B_0 t$

This makes the parameters β' , γ' and f' dimensionless and relative to α . α itself has units of rad s^{-1} and time variable t' has units of $2\pi/\alpha$.

2. Correspondence between classical and quantum Hamiltonian parameters

The above implies that the same convention of a normalized angular momentum has to be followed quantum mechanically. Hence the quantum Hamiltonian \mathcal{H}_q is divided by \hbar and transformed with $\mathbf{I}' = \mathbf{I}/I$, thus converting to frequency units and normalizing the spin operators:

$$\frac{\mathcal{H}_q}{\hbar I} = \gamma_n B_0 I'_z + Q I I'^2_x + \gamma_n B_1 \cos(2\pi f t) I'_y, \quad (\text{D3})$$

This assumes units of Hz T^{-1} for γ_n , units of Hz for Q and dimensionless spin operators \mathbf{I} . Note that after introducing \mathbf{I}' an additional factor I appears in the second term due to its quadratic nature.

Next, as in the classical case, dividing by $\gamma_n B_0$ and introducing time variable $t' = \gamma_n B_0 t$ results in the dimensionless Hamiltonian

$$\begin{aligned} \mathcal{H}'_q &= \frac{\mathcal{H}_q}{\hbar I \gamma_n B_0} = I'_z + \frac{QI}{\gamma_n B_0} I'^2_x + \frac{B_1}{B_0} \cos\left(\frac{2\pi f}{\gamma_n B_0} t'\right) I'_y \\ &= I'_z + Q' I'^2_x + B'_1 \cos(2\pi f' t') I'_y \end{aligned} \quad (\text{D4})$$

Table D 2 gives an overview of the different parameters used throughout the classical and quantum simulations.

Appendix E: Nuclear quadrupole interaction

As discussed in Sec. IV, nuclei with a spin $I > 1/2$ have a quadrupole moment Q_n due to a non-spherical charge distribution.³⁷ This charge distribution has an axis of symmetry that aligns with the nuclear angular momentum and interacts with an electric field gradient (EFG). We estimate the strength of quadrupole interaction due to such an EFG for the different donors in silicon.

For group-V donors in silicon, the EFG is produced by external charges, such as the donor-bound electron or the crystal lattice. In a sample of unperturbed bulk silicon,

the tetrahedral donor symmetry results in canceling EFG components and consequently a vanishing quadrupole interaction in the ground state. In a realistic micro- or nanoelectronic device, strain and/or electric fields can break the bulk symmetry of the donor wave functions.³⁸ Strain is typically present in devices as a result of the mismatch of the coefficient of thermal expansion of different materials, for example between the metal electrodes and semiconductor substrate.^{42,43} The subsequent rearrangement of the multi-valley electron state generates electric field gradients which can couple to the electric quadrupole moment of the donor.^{43,46} Strain also acts on the silicon crystal to produce an EFG through the gradient elastic tensor \mathbf{S} ,⁵⁵ which results in a quadrupole interaction even in the absence of the donor-bound electron.⁴⁵

1. Estimates of Nuclear Quadrupole Interaction

We define the quadrupole interaction strength as the factor that precedes the quadratic $I_{z'}$ term in Eq. 4,

$$Q = \frac{3(1 - \gamma_s)eQ_n V_{z'z'}}{4I(2I - 1)h}. \quad (\text{E1})$$

Here γ_s is the Sternheimer anti-shielding factor, e is the elementary charge, Q_n is the nuclear quadrupole moment, $V_{ij} = \frac{\partial^2 V}{\partial i \partial j}$, ($i, j \in x', y', z'$), are the partial second derivatives of electric potential V , and h is Planck's constant. This differs from the more conventional definition of the quadrupole interaction (by including multiplication factor $3/4I(2I - 1)$), as this allows a direct comparison to the equivalent classical parameter β (App. D). Accurate calculation of Q for donors is complicated by the multiplicative term γ_s . This factor relates to the Sternheimer anti-shielding effect, a phenomenon that describes the re-arrangement of the inner electron shells in response to an external EFG, effectively enhancing the EFG experienced by the nucleus.³⁷ The Sternheimer anti-shielding factor γ_s can be considerable, theoretical calculations⁴⁴ for isolated As and Bi ions show an enhancement of about one order of magnitude for As and up to three orders of magnitude for Bi. To the best of our knowledge, no such calculations have been completed for Sb. Furthermore, it is unknown how the covalent bonding of the donor to the silicon lattice affects γ_s . As a result of the uncertainty in γ_s , it is difficult to make purely theoretical predictions of Q for donors in silicon.

Recent experiments^{43,45–47} on quadrupole effects in silicon devices have produced some quantitative results that can be used to estimate Q for As, Sb and Bi donors in Si. We will present an analysis for each of the donors in sections below, predicting the quadrupole coupling in the ionized charge state D^+ , where the EFG is produced by the crystal lattice alone.

a. Arsenic

Whilst arsenic has the lowest nuclear spin of the donors considered here – making it less-suitable for comparison with classical dynamics – it is a relatively well-studied donor for its quadrupole properties. In Refs. 46 and 45, spectroscopy of As donors in a strained silicon sample has been performed (uni-axial strain $\epsilon_{\perp} \approx 3 \times 10^{-4}$). For an ionized donor, the EFG is generated through the gradient elastic tensor $V = \mathbf{S} \cdot \epsilon$ (where ϵ is the strain tensor in Voigt notation), implying a linear relationship between the applied strain and quadrupole interaction. Measurement of the quadrupole shifts in two samples of different surface planes [(100) and (111)] enabled the extraction of the nontrivial gradient elastic tensor components, $S_{11} = 1.5 \times 10^{22} \text{ V m}^{-2}$ and $S_{44} = 6.8 \times 10^{22} \text{ V m}^{-2}$. These components (which include the Sternheimer anti-shielding factor $\gamma_s \approx -7$ for As⁴⁴) can be used to provide a rough estimation of the D^+ quadrupole coupling for Bi and Sb (see below). In a nano-device, strains of order 10^{-3} are expected directly underneath the metallic surface electrodes⁴² due to the mismatch in thermal expansion coefficients, similar in magnitude to those observed in the pre-strained devices in Refs. 46 and 45. This allows to estimate the quadrupole interaction strength in a device: $Q \approx 210 \text{ kHz}$ for a (111) surface and $Q = 60 \text{ kHz}$ for a (100) surface.

b. Bismuth

In order to estimate Q in the D^+ state for Bi, we require the anti-shielding factor γ_s . We take an order-of-magnitude estimate, only serving as a rough guide, of $\gamma_s \approx 100$ for the anti-shielding factor of Bi. This value is based on the simulations of measured data reported in Refs. 43 and 47.

Using the estimated magnitude of γ_s for Bi, the measured gradient elastic tensor components S_{11} and S_{44} of As (converted to strain using the theoretical magnitude of $|\gamma_s| \approx 7$ for As), we estimate the quadrupole interaction strength achievable in a nano-device for the D^+ state to be: $Q \approx 240 \text{ kHz}$ for a (111) silicon surface and $Q = 45 \text{ kHz}$ for a (100) surface.

c. Antimony

Antimony is the least-understood of the group-V donors for its quadrupole properties. There are no theoretical calculations for the Sternheimer anti-shielding factor, and no experimental data on the interplay between strain and quadrupole interaction. In the EDMR experiments of Ref. 47, Q was found for the neutral ^{121}Sb donor to be approximately half that of the measured value for ^{209}Bi , with the caveat that the implantation conditions were different for the Sb and Bi samples, and no estimate was given for the likely separation between the donors and

the readout centers (which strongly influences the EFG) in the Sb sample.

Appendix F: Hamiltonian characterization via NMR spectroscopy

High-precision measurements of the nuclear-spin Hamiltonian parameters are needed to achieve an accurate comparison between the quantum system and its classical equivalent. Furthermore, this is a crucial requirement in enabling arbitrary state preparation as discussed later (App. G). This section describes how the different parameters can be extracted through NMR spectroscopy of the ionized nucleus.

1. NMR spectroscopy

Starting from a system where none of the NMR transition frequencies are known, the first step is to find the ESR frequency, which uniquely depends on the (unknown) nuclear spin state through the hyperfine coupling. To this end, the electron spin is initialized in the down state through spin-dependent tunneling from the SET island onto the ionized donor, after which a voltage is applied to ensure that the electron is unable to tunnel back. A pulse with linearly-increasing frequency is applied that adiabatically inverts the electron state if its resonance frequency lies within the frequency range.⁵⁶ The bias voltage is then modified to ensure that the electron can only tunnel back onto the SET island if its spin state has successfully been flipped, which is measured as a finite SET current.

Once the first ESR frequency is known, an NMR frequency of the nuclear spin state can be found. The measurement sequence is nearly identical, with the exception that before loading an electron, a voltage is applied to force the donor into the ionized state, followed by another pulse with linearly-increasing frequency in the expected NMR frequency range. If this pulse sweeps over one of the active NMR frequencies, this will adiabatically invert the nuclear spin state. As a result, the ESR frequency will change, and so no subsequent adiabatic inversion of the electron spin state will occur. Repeating the measurement flips the nuclear spin state, resulting in an alternating electron spin flip probability, allowing determination of the NMR frequency. The previous two steps can then be repeated to iteratively determine all ESR and NMR frequencies.

The above scheme assumes that loading/unloading an electron leaves the nuclear-spin eigenstates intact, which may require an adiabatic electron-loading scheme (App. G).

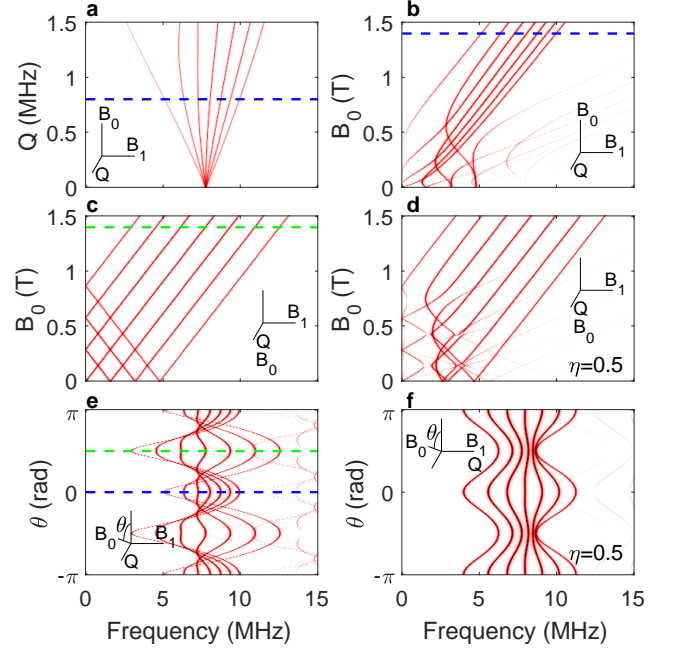


Figure 7. NMR spectra of the ionized ^{123}Sb donor ($I = 7/2$). In all panels, the transition line intensities indicate the coupling between corresponding states, and parameter orientations are given by coordinate axes. Blue and green dashed lines each indicate matching conditions across panels. Unless specified otherwise, the Hamiltonian is given by Eq. (5), with $B_0 = 1.4\text{ T}$, $Q = 0.8\text{ MHz}$, and $\eta = 0$ (blue dashed lines). (a) Influence of Q on NMR spectra for perpendicular orientations of B_0 , Q , and B_1 . The convergence of NMR transition frequencies for $Q = 0\text{ Hz}$ shows that a nonzero quadrupole is necessary to distinguish NMR transitions. (b) Influence of B_0 on NMR spectra for perpendicular orientations of B_0 , Q , and B_1 . In the absence of a linear interaction ($B_0 = 0\text{ T}$), the two-fold degeneracy of the quadratic interaction translates to 3 distinct NMR frequencies. This degeneracy is lifted when $B_0 > 0\text{ T}$, and the transition frequencies approach a linear dependence on B_0 in the high-field regime. (c) B_0 is varied while oriented along the principal quadrupole axis \hat{z}' . In this case, the eigenstates of the Zeeman interaction are simultaneously eigenstates of the quadrupole interaction, resulting in a linear dependence on B_0 and a constant spacing of $2Q$ between successive transitions. (d) Same as (c) but with $\eta = 0.5$, which results in a nonlinear NMR-frequency dependence on B_0 . The behavior of (c) is recovered in the large-field limit ($Q \ll \gamma_n B_0$). (e) Rotating B_0 towards principal quadrupole interaction axis, revealing a π -periodicity and two symmetry axes. The separation of NMR frequencies is maximal when the orientations of B_0 and Q are aligned. (f) Rotating B_0 perpendicular to Q with $\eta = 0.5$. The separation between spectral lines is maximal when B_0 is aligned with the secondary quadrupole interaction axis y' . When $\eta = 0$, there is no dependence of spectral lines upon rotating B_0 perpendicular to Q .

2. Extraction of Hamiltonian parameters

Combining NMR spectroscopy with full control of both the direction and strength of B_0 allows extraction of all Hamiltonian parameters. This relies on the underlying assumption that each of the NMR transitions is individually addressable, a condition that can be satisfied by assuming a Q larger than the NMR transition linewidth (Fig. 7a). It eases analysis to operate in the large magnetic field limit ($Q \ll \gamma_n B_0$), where the quadrupole interaction can be treated as a perturbation to Eq. 3 (Fig. 7b).

The first goal is to determine the orientation of the quadrupole coordinate system $(\hat{x}', \hat{y}', \hat{z}')$ (Eq. 4). Once known, aligning the B_0 -axis with \hat{z}' provides the strength of Q , since successive NMR transitions have a constant separation of $2Q$ (Fig. 7c). This equidistant spacing is lifted by a nonzero asymmetry parameter ($\eta > 0$), but is recovered in the high magnetic-field limit (Fig. 7d).

The quadrupole's primary axis \hat{z}' can be found through successive spectroscopy measurements while rotating B_0 . Without prior knowledge of the quadrupole's coordinate system, B_0 is initially rotated around an arbitrary axis. It is guaranteed that such a spectroscopy will reveal two symmetry axes, one of which is perpendicular to \hat{z}' . A second rotation of B_0 around this particular symmetry axis will align B_0 with \hat{z}' at some specific angle. This point has maximum and (nearly) equidistant separation of the spectral lines, thereby revealing the quadrupole's primary axis \hat{z}' (Fig. 7e).

The two remaining unknown parameters of the quadrupole interaction, the asymmetry η and its orientation, can be found through a final rotation of B_0 around the \hat{z}' -axis. If $\eta = 0$, spectral lines will be independent of this rotation, while for $\eta > 0$ again two symmetry axes will be revealed. The symmetry axes with the largest separation of spectral lines corresponds to B_0 being parallel to the secondary \hat{y}' -axis, and the strength of spectral line variation is determined by the size of η (no analytic expression).

The sequence sketched here allows variation of a single experimental handle (NMR frequency, B_0 direction) to isolate the effect of each parameter. This allows an accurate determination of all the relevant Hamiltonian parameters and a detailed understanding of the system.

Appendix G: State preparation and measurement

1. Arbitrary state preparation

The ability to create an arbitrary target state $|\psi_T\rangle$ requires addressability of individual transition frequencies and accurate knowledge of all Hamiltonian parameters. The procedure described in this section can be used for arbitrary state preparation, provided that the above conditions are fulfilled.

Assuming the system to be initialized in the ground

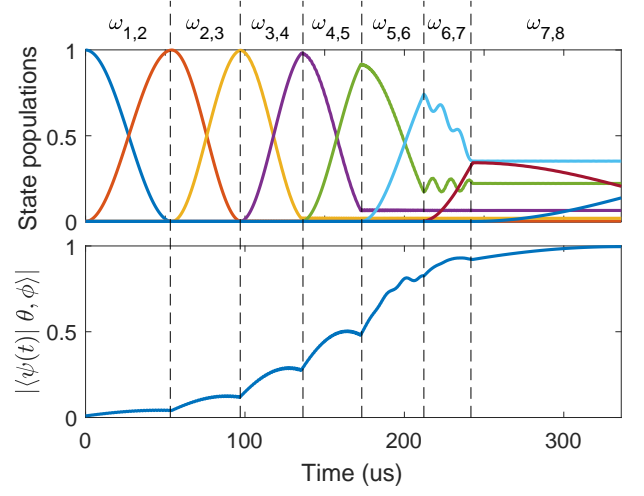


Figure 8. Preparation of spin coherent state $|\theta, \phi\rangle = |4\pi/5, \pi/2\rangle$, starting from the ground state. A succession of pulses with different frequencies $f_{k,k'}$ iteratively transfer population from lower-energy eigenstates $|e_k\rangle$ to higher-energy eigenstate $|e_{k'}\rangle$. To account for the remaining phase accumulation, intermediate fidelities were calculated after leaving the intermediate state idle until the end of the sequence. The final fidelity between evolved state and target spin coherent state is $|\langle\psi|\theta, \phi\rangle| = 0.996$ for $B_1 = 1$ mT, $Q = 1$ MHz, $B_0 = 0.7$ T, and can be further increased by reducing the oscillating magnetic-field strength.

state $|e_1\rangle$, the necessary sequence of pulses that results in the target state $|\psi_T\rangle$ can be found by solving the problem in reverse: go backwards in time and find the pulse sequence to end up in $|e_1\rangle$ starting from $|\psi_T\rangle$. Starting at $t = 0$ s with initial state $|\psi_T\rangle = \sum_k a_k |e_k\rangle$, where $a_k = \langle e_k | \psi_T \rangle$, pulses are iteratively chosen that transfer population from the populated highest-energy eigenstate to a lower-energy eigenstate. The procedure is as follows:

1. Choose eigenstate $|e_k\rangle$ with highest eigenvalue λ_k and nonzero population $|a_k|$.
2. Find eigenstate $|e_{k'}\rangle$ with lower eigenvalue $\lambda_{k'}$ that has the highest coupling $|\langle e_{k'} | I_y | e_k \rangle|$.
3. Transfer the population from $|e_k\rangle$ to $|e_{k'}\rangle$ using a pulse with the following properties:
 - frequency $f_{k,k'}$, which is the transition frequency between $|e_k\rangle$ and $|e_{k'}\rangle$;
 - duration $t_p = \frac{\pi}{\Omega_{k,k'}} \frac{|a_k|^2}{\sqrt{|a_k|^2 + |a_{k'}|^2}}$, where $\Omega_{k,k'}$ is the Rabi frequency;
 - phase is the relative phase difference between a_k and $a_{k'}$, minus the phase offset $2\pi f_{k,k'}(t - t_p)$.
4. Update $t \rightarrow t - t_p$ and repeat steps until all population is transferred to $|e_1\rangle$.

These steps can be followed to create an arbitrary pure state, and in particular the spin coherent states $|\theta, \phi\rangle$ used in the proposed quantum driven-top experiments. While we do not expect our state-preparation fidelity to be limited by effects such as decoherence, the total pulse-sequence duration can be further reduced by using multi-frequency pulses.

2. Measurement

The presence of a strong quadrupole interaction with axis perpendicular to that of the linear interaction inhibits defining a clear quantization axis. Upon adding an electron to the ionized donor, the accompanying hyperfine interaction can be approximated as an enhancement of the linear interaction by about an order of magnitude for ^{123}Sb (two orders for ^{209}Bi), significantly altering the eigenbasis of the donor. The existing techniques for initialization and readout of the nucleus rely on electron tunneling events between donor and SET island. Here, these tunneling events are accompanied by a change of eigenbasis, resulting in a probabilistically-modified state after every such event. Modified protocols may therefore be necessary for high-fidelity nuclear state initialization and readout.

The proposed solution is the adiabatic transferring of the electron from donor to the silicon/siliconoxide interface, which maps neutral-donor eigenstates to ionized-donor eigenstates and vice versa. This can be achieved by the addition of an electrostatic gate above the donor that can attract its outer electron, a technique that is being developed in the context of achieving electrically active transitions and long-range coupling of donor qubits [ref.](#) Once the electron is removed from the donor to the interface, spin dependent tunneling of the electron from interface to SET island allows for read-out without affecting the nucleus.

Appendix H: Numerical methods and simulation details

Both the classical and quantum simulations were primarily performed using the commercial software package MATLAB Release 2016b, The MathWorks, Inc., Natick, Massachusetts, United States. In this section we will describe the simulation techniques for both the classical and the quantum simulations.

1. Classical simulations

The most computationally expensive simulations were those to determine the percentage of phase space that is chaotic (Fig. 1h, i). Both colormaps consist of 25×25 logarithmically-spaced points, each of which corresponds to a particular parameter set. For each parameter set, a

total of 2000 initial angular-momentum coordinates were chosen uniformly-distributed over the phase space. To determine if the dynamics of an initial coordinate is chaotic, a neighboring point with distance 10^{-8} was chosen, and both were evolved for a fixed duration of $100/\alpha$. Whether or not a trajectory is chaotic is determined by measuring the distance between the two points over time, and fitting this to an exponential curve. Chaos is characterized by an exponential sensitivity to perturbations, and so the trajectory is categorized as chaotic if its exponent is above a certain threshold. This procedure is repeated for each of the 2000 initial conditions, resulting in the percentage of phase space that is chaotic.

Some trajectories, especially near a chaotic-regular boundary, can display an initial exponential divergence but nevertheless behave regular over sufficient evolution time. These cases, although uncommon, can result in the trajectory being wrongly categorized as chaotic, and we expect a small uncertainty in the percentages of Fig. 1h, i. It should furthermore be noted that the fitted exponent is not necessarily equal to the Lyapunov exponent, as the inter-trajectory distance may have increased sufficiently to be limited by the finite size of the phase space. Although the exponent is then an underestimate of the Lyapunov exponent, it will for certain be above the chaotic threshold, thereby correctly characterizing the trajectory as chaotic.

The classical simulation results shown in Fig. 1 were obtained using the ordinary-differential-equation (ODE) solver SUNDIALS.⁵⁷ Communication between MATLAB and Sundials was through self-written C code that was optimized for the driven-top system. The combination of SUNDIALS and the intermediate C code resulted in a computational speedup of over an order of magnitude compared to the native MATLAB ODE solvers. As chaotic dynamics are highly sensitive to perturbations, stringent error tolerances were chosen to ensure a high degree of accuracy in the computation of the trajectories.

2. Quantum simulations

The quantum driven-top system is evolved using the Floquet operator F , which can be approximated through segmentation as

$$F \approx \prod_{k=0}^N e^{i \frac{t}{N} \mathcal{H}(\frac{k}{N})/\hbar}, \quad (\text{H1})$$

which becomes an equality in the limit $N \rightarrow \infty$. In the simulations, a fixed value of $N = 1000$ is used, as results showed that the Floquet operator did not significantly change upon further increasing N . Additionally, the SUNDIALS ODE solver was used to compute F , and was found to be nearly identical to F computed using the above method.

Decoherence of spin coherent states under influence of the driven-top Hamiltonian (Eq. 5) was simulated by randomly fluctuating a Hamiltonian parameter during

its evolution and averaging over many such evolutions. To this end, Floquet operators were calculated for 30 values of Q uniformly distributed within three standard deviations of its mean value ($Q = 800(2)$ kHz). For the evolution, a sequence of Floquet operators were chosen

through random sampling of this set using a Gaussian distribution. This sequence was then applied to all initial spin coherent states, and this process was repeated for 300 such sequences. For each spin coherent state, the final density matrices were averaged, resulting in a mixed state ρ , from which the purity $\text{Tr}(\rho^2)$ was determined.

-
- * These authors contributed equally.
- ¹ A. J. Leggett, *Journal of Physics: Condensed Matter* **14**, R415 (2002).
 - ² W. H. Zurek, *Reviews of modern physics* **75**, 715 (2003).
 - ³ M. Schlosshauer, *Reviews of Modern physics* **76**, 1267 (2005).
 - ⁴ G. Casati and B. Chirikov, *Physica D: Nonlinear Phenomena* **86**, 220 (1995).
 - ⁵ H. Korsch and M. Berry, *Physica D: Nonlinear Phenomena* **3**, 627 (1981).
 - ⁶ M. V. Berry, in *Proceedings of the Royal Society of London A: Mathematical, Physical and Engineering Sciences*, Vol. 413 (The Royal Society, 1987) pp. 183–198.
 - ⁷ M. Srednicki, *Physical Review E* **50**, 888 (1994).
 - ⁸ M. Rigol, V. Dunjko, and M. Olshanii, *Nature* **452**, 854 (2008).
 - ⁹ J. Eisert, M. Friesdorf, and C. Gogolin, *Nature Physics* **11**, 124 (2015).
 - ¹⁰ W. H. Zurek and J. P. Paz, *Physical Review Letters* **72**, 2508 (1994).
 - ¹¹ B. Georgeot and D. L. Shepelyansky, *Physical Review E* **62**, 3504 (2000).
 - ¹² P. Silvestrov, H. Schomerus, and C. Beenakker, *Physical review letters* **86**, 5192 (2001).
 - ¹³ D. Braun, *Physical Review A* **65**, 042317 (2002).
 - ¹⁴ C. Marcus, A. Rimberg, R. Westervelt, P. Hopkins, and A. Gossard, *Physical review letters* **69**, 506 (1992).
 - ¹⁵ P. Wilkinson, T. Fromhold, L. Eaves, F. Sheard, *et al.*, *Nature* **380**, 608 (1996).
 - ¹⁶ W. K. Hensinger, H. Häffner, A. Browaeys, N. R. Heckenberg, K. Helmerson, C. McKenzie, G. J. Milburn, W. D. Phillips, S. L. Rolston, H. Rubinsztein-Dunlop, *et al.*, *Nature* **412**, 52 (2001).
 - ¹⁷ S. Chaudhury, A. Smith, B. Anderson, S. Ghose, and P. S. Jessen, *Nature* **461**, 768 (2009).
 - ¹⁸ I. Manai, J.-F. Clément, R. Chicireanu, C. Hainaut, J. C. Garreau, P. Szriftgiser, and D. Delande, *Physical review letters* **115**, 240603 (2015).
 - ¹⁹ C. Neill, P. Roushan, M. Fang, Y. Chen, M. Kolodrubetz, Z. Chen, A. Megrant, R. Barends, B. Campbell, B. Chiaro, *et al.*, *Nature Physics* **12**, 1037 (2016).
 - ²⁰ B. Sanders and G. Milburn, *Zeitschrift für Physik B Condensed Matter* **77**, 497 (1989).
 - ²¹ J. K. Eastman, J. J. Hope, and A. R. Carvalho, *arXiv preprint arXiv:1604.03494* (2016).
 - ²² F. Haake, *Journal of Modern Optics* **47**, 2883 (2000).
 - ²³ K. M. Itoh and H. Watanabe, *MRS Communications* **4**, 143 (2014).
 - ²⁴ B. E. Kane, *Nature* **393**, 133 (1998).
 - ²⁵ A. Morello, J. J. Pla, F. A. Zwanenburg, K. W. Chan, K. Y. Tan, H. Huebl, M. Möttönen, C. D. Nugroho, C. Yang, J. A. van Donkelaar, *et al.*, *Nature* **467**, 687 (2010).
 - ²⁶ J. J. Pla, K. Y. Tan, J. P. Dehollain, W. H. Lim, J. J. Morton, F. A. Zwanenburg, D. N. Jamieson, A. S. Dzurak, and A. Morello, *Nature* **496**, 334 (2013).
 - ²⁷ J. J. Pla, K. Y. Tan, J. P. Dehollain, W. H. Lim, J. J. Morton, D. N. Jamieson, A. S. Dzurak, and A. Morello, *Nature* **489**, 541 (2012).
 - ²⁸ J. P. Dehollain, S. Simmons, J. T. Muhonen, R. Kalra, A. Laucht, F. Hudson, K. M. Itoh, D. N. Jamieson, J. C. McCallum, A. S. Dzurak, *et al.*, *Nature Nanotechnology* **11**, 242 (2016).
 - ²⁹ J. Muhonen, J. Dehollain, A. Laucht, S. Simmons, R. Kalra, F. Hudson, D. Jamieson, J. McCallum, K. Itoh, A. Dzurak, *et al.*, *arXiv preprint arXiv:1702.07991* (2017).
 - ³⁰ J. Van Donkelaar, C. Yang, A. Alves, J. McCallum, C. Hougaard, B. Johnson, F. Hudson, A. Dzurak, A. Morello, D. Spemann, *et al.*, *Journal of Physics: Condensed Matter* **27**, 154204 (2015).
 - ³¹ J. T. Muhonen, J. P. Dehollain, A. Laucht, F. E. Hudson, R. Kalra, T. Sekiguchi, K. M. Itoh, D. N. Jamieson, J. C. McCallum, A. S. Dzurak, *et al.*, *Nature nanotechnology* **9**, 986 (2014).
 - ³² J. Muhonen, A. Laucht, S. Simmons, J. Dehollain, R. Kalra, F. Hudson, S. Freer, K. M. Itoh, D. Jamieson, J. McCallum, *et al.*, *Journal of Physics: Condensed Matter* **27**, 154205 (2015).
 - ³³ J. P. Dehollain, J. T. Muhonen, R. Blume-Kohout, K. M. Rudinger, J. K. Gamble, E. Nielsen, A. Laucht, S. Simmons, R. Kalra, A. S. Dzurak, *et al.*, *New Journal of Physics* **18**, 103018 (2016).
 - ³⁴ G. Wolfowicz and J. J. L. Morton, *eMagRes* (2007).
 - ³⁵ M. Veldhorst, J. C. C. Hwang, C. H. Yang, A. W. Leenstra, B. De Ronde, J. P. Dehollain, J. T. Muhonen, F. E. Hudson, K. M. Itoh, A. Morello, and A. S. Dzurak, *Nature nanotechnology* **9**, 981 (2014).
 - ³⁶ .
 - ³⁷ E. N. Kaufmann and R. J. Vianden, *Reviews of Modern Physics* **51**, 161 (1979).
 - ³⁸ C. P. Slichter, “Principles of magnetic resonance,” (Springer-Verlag, 1990) Chap. 10, pp. 494–502, 3rd ed.
 - ³⁹ A. Ramdas and S. Rodriguez, *Reports on Progress in Physics* **44**, 1297 (1981).
 - ⁴⁰ G. Feher, *Physical Review* **114**, 1219 (1959).
 - ⁴¹ N. J. Stone, *Int. Nucl. Data Committee, document INDC (NDS)-0658* (2014).
 - ⁴² T. Thorbeck and N. M. Zimmerman, *AIP Advances* **5**, 087107 (2015).
 - ⁴³ J. J. Pla, A. Bienfait, G. Pica, J. Mansir, F. A. Mohiyaddin, A. Morello, T. Schenkel, B. W. Lovett, J. J. L. Morton, and P. Bertet, *arXiv preprint arXiv:1608.07346* (2016).
 - ⁴⁴ F. D. Feiock and W. R. Johnson, *Physical Review* **187**, 39 (1969).
 - ⁴⁵ D. P. Franke, F. M. Hrubesch, M. Künzli, H.-W. Becker, K. M. Itoh, M. Stutzmann, F. Hoehne, L. Dreher, and M. S. Brandt, *Physical Review Letters* **115**, 057601 (2015).

- ⁴⁶ D. P. Franke, M. P. Pflüger, P.-A. Mortemousque, K. M. Itoh, and M. S. Brandt, [Physical Review B](#) **93**, 161303 (2016).
- ⁴⁷ P. A. Mortemousque, S. Rosenius, G. Pica, D. P. Franke, T. Sekiguchi, A. Truong, M. P. Vlasenko, L. S. Vlasenko, M. S. Brandt, R. G. Elliman, and K. M. Itoh, [Nanotechnology](#) **27**, 494001 (2016).
- ⁴⁸ S. E. Thompson, G. Sun, Y. S. Choi, and T. Nishida, [IEEE Transactions on Electron Devices](#) **53**, 1010 (2006).
- ⁴⁹ L. Dreher, T. A. Hilker, A. Brandlmaier, S. T. Goennenwein, H. Huebl, M. Stutzmann, and M. S. Brandt, [Physical Review Letters](#) **106**, 037601 (2011).
- ⁵⁰ T. Schenkel, J. Liddle, A. Persaud, A. Tyryshkin, S. Lyon, R. De Sousa, K. B. Whaley, J. Bokor, J. Shangkuan, and I. Chakarov, [Applied Physics Letters](#) **88**, 112101 (2006).
- ⁵¹ C. Weis, C. Lo, V. Lang, A. Tyryshkin, R. George, K. Yu, J. Bokor, S. Lyon, J. Morton, and T. Schenkel, [Applied Physics Letters](#) **100**, 172104 (2012).
- ⁵² G. Tosi, F. A. Mohiyaddin, S. B. Tenberg, R. Rahman, G. Klimeck, and A. Morello, [arXiv preprint arXiv:1509.08538v2](#) (2015).
- ⁵³ K. Murch, S. Weber, C. Macklin, and I. Siddiqi, [Nature](#) **502**, 211 (2013).
- ⁵⁴ F. T. Arecchi, E. Courtens, R. Gilmore, and H. Thomas, [Phys. Rev. A](#) **6**, 2211 (1972).
- ⁵⁵ R. K. Sundfors, [Physical Review B](#) **20**, 3562 (1979).
- ⁵⁶ A. Laucht, R. Kalra, J. T. Muhonen, J. P. Dehollain, F. A. Mohiyaddin, F. Hudson, J. C. McCallum, D. N. Jamieson, A. S. Dzurak, and A. Morello, [Applied Physics Letters](#) **104**, 092115 (2014).
- ⁵⁷ A. C. Hindmarsh, P. N. Brown, K. E. Grant, S. L. Lee, R. Serban, D. E. Shumaker, and C. S. Woodward, [ACM Transactions on Mathematical Software \(TOMS\)](#) **31**, 363 (2005).